Photonic integrated beam delivery in a rubidium 3D magneto-optical trap

Andrei Isichenko[1], Nitesh Chauhan[1], Debapam Bose[1], Jiawei Wang[1], Paul D. Kunz[2], and Daniel J. Blumenthal[1*]

[1] Department of Electrical and Computer Engineering, University of California Santa Barbara, Santa Barbara, CA 93106 USA

[2] U.S. Army Research Laboratory, Adelphi, MD 20783 USA

* Corresponding author (danb@ucsb.edu)

ABSTRACT

Cold atoms are central to precision atomic applications including timekeeping and sensing. The 3D magneto-optical trap (3D-MOT), used to produce a cloud of cold atoms, will benefit from photonic waveguide integration to improve reliability and reduce size, weight, and cost. These traps require the delivery of multiple, large area, collimated laser beams to an atomic vacuum cell. Yet, to date, beam delivery using an integrated waveguide approach has remained elusive. We report demonstration of a ^{87}Rb 3D-MOT using a fiber-coupled photonic integrated circuit to deliver all necessary beams to cool and trap more than 5 x 10^6 atoms to near 200 μK in a trapping volume that is an order of magnitude smaller than that of an equivalent atom number diffraction grating MOT. The silicon nitride photonic circuit transforms fiber-coupled 780 nm cooling and repump light via waveguides to three orthogonal non-diverging 2.5 mm x 3.5 mm free-space cooling and repump beams directly interface to the rubidium cell. This full planar, CMOS foundry-compatible integrated beam delivery is compatible with other components, such as lasers and modulators, promising system-on-chip solutions for cold atom applications.

INTRODUCTION

Cold atoms[1–4] are a central component of precision scientific tools including atomic clocks[5–8] and ultra-high resolution spectroscopy[9–11] and form the basic building blocks for applications such as atomic timekeeping[12], quantum computing[13–17], and quantum sensing[18–20] by enabling improved spectroscopy resolution for observing the quantum behavior of atoms[3]. Today's atom trapping and cooling systems employ free-space lasers and optics that occupy tables and racks and are costly and power consuming. Realizing these systems at the chip-scale, with a complementary oxide semiconductor (CMOS) foundry-compatible photonic integrated circuit (PICs) process will improve their reliability, lower their cost, and enable portability[18,21] and new cold-atom systems for applications such as mobile gravity mapping[19] and space-based atomic clocks[22].

The three-dimensional (3D) magneto-optical trap (MOT)[1–4, 23–28], in particular, is a widely used configuration to directly create a large population of trapped and cooled atoms. The trap is formed inside vacuum environment using a balance of optical radiation forces via six cooling beams and a magnetic field gradient with a null located at the beam intersection of the cooling beams[23]. As the trapped atom number scales strongly with the beam diameter, beam diameters of at least 1 mm are needed to trap and cool over 1 million cold atoms as is desired for improved application sensitivity[29,30]. Efforts to miniaturize[30] the beam delivery components in a MOT have primarily focused on micro-optic reflective components such as pyramidal mirrors[31,32] or diffraction gratings[33–37] to convert a collimated free-space input beam into multiple intersecting beams. Diffraction grating MOTs (GMOTs) have emerged as a robust candidate and have recently been demonstrated in a compact sensor for atom interferometry[20]. Further MOT size reduction efforts employed micro-fabricated pyramids etched into silicon[38], but have the tradeoff of a small beam overlap volume that limits the atom number. Free-space illuminated meta-surface structures capable of high efficiency MOT beam delivery[39] utilize bulk optic components for beam expansion and involve complex electron-beam lithography during fabrication. These approaches require bulk free-space optic components for beam expansion and the distance required for expansion optics poses a limit to the minimum size of the MOT package. Photonic integrated circuit (PIC) technology in the silicon nitride (Si_3N_4) platform[40] offers a rich set of passive and active components with low optical losses and compatibility with CMOS foundry processes at cold atom visible wavelengths[41–43]. To date, Si_3N_4 PICs have been used to demonstrate transformation of 780 nm light from a waveguide to a free-space beam via an on-chip surface grating, producing a free-space beam diameter of 320 um[44] and 3 mm[45] and used as a probe beam in a rubidium spectroscopy reference[46] and micrometer-size focused beams for ion-trap quantum computing[47]. Recently, a meta-surface beam expander above a single PIC emitter was used to generate a diverging, cm-size beam as the input for a GMOT[36]. However, to date, 3D-MOT atom cooling using an integrated waveguide to free-space beam delivery system has not been reported.

In this work we demonstrate for the first time, to the best of our knowledge, laser cooling and trapping of ^{87}Rb atoms in a 3D-MOT using a photonic integrated fiber-coupled photonic chip for the delivery of cooling and repump beams directly to a rubidium vapour cell. This photonic integrated circuit (PIC) enables a 3D-PICMOT, based on a CMOS foundry compatible Si_3N_4 waveguide circuit[40] for fiber coupling, beam expansion, collimation, and delivery to the vapour cell. The PIC transforms fiber-coupled 780 nm cooling and repump light into three 2.5 mm x 3.5 mm ($1/e^2$ diameter) collimated free-space beams[45] producing a beam overlap volume of 17 mm^3 inside the vapour cell at a height 9 mm above the PIC surface. Using this PIC delivery interface, we measure a MOT cloud of ~5 x 10^6 atoms and a temperature near 200 μK using time of flight

(TOF) and release-and-recapture (RR) temperature measurements. We achieve the same atom number as a GMOT in an order of magnitude smaller beam overlap volume[20,34]. The PIC supports delivery of intensities of over 3 I_{sat} (where $I_{sat} = 3.6$ mW/cm^2 for the [87]Rb $D2$ transition) per cooling beam owing to the low absorption and the high-power handling capability of the Si$_3$N$_4$ waveguides. The power loss from the fiber input to the sum of the free-space emitted beams is 15.8 dB, which includes the loss from the packaged fiber input, excess loss of the 1x3 splitter, waveguide and mode transformer, and grating losses. Strategies to reduce this loss below 8 dB are discussed. This integrated beam delivery approach can be designed to support wavelengths from 405 nm – 2350 nm[41] and can be integrated with other key active and passive components[48–51], including lasers[52], ultra-low power consumption modulators[51], and reference cavities[53], to further reduce the size of 3D-MOTs. The system can be designed for operation at wavelengths for different atom species including, for example, neutral strontium (atomic clock transitions in the range from 461nm - 813 nm[6]) and cesium (MOTs at 852 nm[54]). These results show promise for the next generation of ultra-compact, energy efficient, and portable cold atom systems.

RESULTS

PICMOT system design and assembly

A diagram of the laser cooling beam delivery PIC configured in a 3D-MOT is shown schematically in Figure 1. The MOT laser light is generated with two independent lasers, cooling (780.241 nm) and repump (780.228 nm), combined using a fiber directional coupler, and packaged using epoxy to the PIC input waveguide. Two current-carrying anti-Helmholtz coils are aligned along one beam axis as shown to form a quadrupole magnetic field with a null at the beam intersection within the vapour cell. The quarter waveplates (QWPs) are mounted directly above the chip and are rotated such that the circular polarization handedness of beams B1 and B3 is opposite that of B2. Three retroreflectors, each containing a mirror and quarter waveplate, are used to produce the other three of the six MOT trapping beams with the correct polarization states.

The PIC delivers non-diverging cooling and repump beams that intersect at a height of 9.45 mm above the PIC surface. This allows the PIC to be located outside of the glass vacuum cell and provide a compact configuration. The cell containing the rubidium atoms is a ColdQuanta™ rubidium miniMOT. A key novel feature of our design that makes the MOT more compact, is that the PIC delivers all beams through the same glass cell wall, which is a different than typical 3D-MOTs that deliver one beam per glass wall. To reduce stray reflections and higher order modes, we use a matte-black aluminum foil baffle layer above the quarter wave plates. The retroreflector mirrors are aligned above the cell to form overlapping counter-propagating beams. The magnetic field is set by adjusting the relative current in each coil and with external magnets for field-shimming.

Laser cooling and repump beam delivery PIC

The 3D-MOT beam delivery PIC is based on a low-loss Si$_3$N$_4$ core and SiO$_2$ cladding single mode waveguide designed to operate at 780 nm (cross section shown in Supplementary Figure 2(a). The cooling and repump laser light is coupled via a single mode optical fiber to a single mode waveguide at the PIC input as shown in Fig. 2. The fiber-coupled input is waveguided to a 1 x 3 multimode interference (MMI) waveguide splitter with each output routed to one of three slab

waveguide beam expanders, each uniformly illuminating one of three large-area surface grating emitters[45]. The grating emitter free-space collimated beams are designed to cool a large volume of rubidium atoms as well as provide a good beam intensity uniformity. The grating centers are positioned on a 13.5 mm diameter circle. Each emits a collimated beam at an angle of 57° from the PIC surface normal (Fig. 2(a)) towards the circle center, producing a 93° intersection between all three beams at a point 9.45 mm above the chip surface. The output of each grating emitter is linearly polarized. Individual 10 mm diameter quarter waveplates are located directly above each grating emitter to convert to the circular polarization required for generating the MOT (see Methods). A photograph of the PIC fiber-coupled with red laser light is shown in Fig. 2(b).

The PIC emits collimated free-space beams with a large cross-sectional area of 8.75 mm². This corresponds to a record large on-chip optical mode expansion factor of 20×10^6 from the 0.44 µm² area waveguided mode delivered to an operational 3D-MOT. We use a CMOS camera to image the beams incident on a screen located above the PIC surface (Fig. 2(c)). From the beam intensity cross section at a distance 5 mm away from the PIC emitter the measured beam width (defined as the $1/e^2$ diameter) dimensions are 2.5 mm by 3.5 mm (Fig. 2(d)) which corresponds to a trapping beam overlap volume of 17.3 mm³. By measuring the beam widths at different distances above the PIC surface we calculate divergence angles 0.16° and 0.35° for the x and y axes, respectively. This corresponds to M^2 values of 10 and 15 in the x and y axes, respectively, characteristic of flat-top beams. It has been shown that trapping beams of a more uniform, flat-top intensity can achieve higher MOT atom numbers than gaussian beams due to the increased optical forces near the edges of the beam overlap volume[36]. We measure root-mean-squared (RMS) intensity variations to be <9% in the central 20% of the mode area and 12% in the central 80% of the mode area. Furthermore, the effective Rayleigh lengths (z_R/M^2) are 125 cm and 113 cm and the beam dimension aspect ratio changes by 20% over 35 cm (Supplementary Information Fig. 2). This good collimation enables placing the grating emitters further apart on the PIC layout to achieve a larger beam intersection height if necessary. The large beam size is possible due to the combination of the large width and low loss of the slab expander and the shallow etch of the grating emitter. Details of the design and fabrication of the waveguides, beam expanders, and grating emitters are given in the Methods section and Supplementary Information.

The average power loss from the fiber input to each free-space beam output is 21.4 dB, corresponding to a total optical loss of beam delivery (fiber input to the sum of the beams) of 15.8 dB. These losses include the fiber to waveguide, splitter, and waveguide propagation losses. We discuss paths forward to reduce this loss factor to below 8 dB in Supplementary Information Note 4. The beams (labeled B1, B2, B3) have a relative power of 28%, 28%, 44% of the input power, producing no noticeable change in PICMOT operation. For an input fiber power 80 mW the PIC delivers an average power of 0.58 mW per cooling beam, corresponding to a beam intensity of 6.6 mW/cm², or 1.8 I_{sat} (for $I_{sat} = 3.6$ mW/cm²). A summary of the loss contributions from the PIC is in Supplementary Information Table 1.

Rubidium atom cooling demonstration

We demonstrate an operational [87]Rb 3D-MOT using this interface. Laser cooling light at 780.24 nm is prepared by stabilizing the cooling laser relative to a hyperfine transition on the [87]Rb D_2 line using an external saturation absorption spectroscopy setup and a separate repumping laser is aligned to the $F = 1 \rightarrow F' = 2$ transition[24] (see Methods). The cooling laser detuning Δ is

controlled with an acousto-optical frequency shifter (AOFS). The axial magnetic field gradient is 20 G/cm through the trap center.

The resulting cloud of trapped ^{87}Rb atoms is shown in Figure 4(a). The beams emitted from the PIC fluoresce as they propagate through the vacuum cell. The inset in Fig. 4(a) shows a close-up image of the MOT cloud. From similar images where the camera pixels in the region of the cloud are not saturated, we estimate a cloud gaussian diameter of 0.4 mm. The steady-state population of the MOT is measured by collecting the cloud fluorescence onto a photodiode (see Methods). With an input power of 150 mW into the PIC fiber input we achieve an atom number of ~5 x 10^6 with the cooling laser red-detuned by 12.6 MHz. The exponential time constant for the MOT loading is measured to be 0.3 s by fitting to data (see Supplementary Information Fig. 3).

The temperature of the trapped atom cloud is evaluated using the widely-used absorption imaging time-of-flight (TOF)[55,56] technique. We also employ an alternate release-and-recapture (RR) method to independently validate the results[57]. In both measurements, the cooling and repump beams are turned off in <5 μs (see Methods). The temperature is extracted based on the free-expansion of the cloud and assuming a Maxwell-Boltzmann velocity distribution of the atoms[55]. For TOF, a free-space beam resonant with the ^{87}Rb cooling transition was externally routed to probe the MOT and the shut-off of the optical and magnetic fields were synchronized. The cloud widths were extracted from pairs of absorption images I_1 and I_2, where I_1 is the image of the probe flashed (duration 0.5 ms) at a time t_{TOF} after the MOT shut-off and I_2 is recorded at $t_{TOF} + 70$ ms when the MOT has dissipated. The optical depth (OD) is extracted using the equation $OD = \ln((I_2 - I_1)/I_2)$ and a Gaussian fit along each axis is taken to extract the width of the cloud. By measuring flight times t_{TOF} up to 1.25 ms, we extract temperature of 185$\pm$17 μK and 221$\pm$36 μK in the y and z axes, respectively. The RR method resulted in a conservative temperature of 400$\pm$200 μK which serves as an upper bound of the cloud temperature due to an overestimate in defining the boundary of where the atoms can be recaptured. The measured temperature is close to the ^{87}Rb D_2 line Doppler cooling limit of 146 μK[58] and the different temperature for each axis in each axis is due to the imbalance of forces in the MOT and different magnetic field shimming conditions. Lower, sub-Doppler-limit MOT temperatures could be achieved with additional cooling stages such as polarization-gradient cooling.

DISCUSSION

In this paper, we demonstrate the laser cooling and trapping of ^{87}Rb atoms using a fiber-coupled silicon nitride photonic integrated circuit that is directly interfaced to a 3D-MOT and delivers both cooling and repump light to an adjacent rubidium vacuum cell. The laser beam delivery PIC achieves a record waveguide free space beam expansion factor of 20 x 10^6 for an operational 3D-MOT. The three output beams have a large area of 2.5 mm x 3.5 mm and are emitted at an angle of 57° to the PIC normal and intersect nearly orthogonally at a point 9.45 mm above the PIC surface. We achieve cooling and trapping of greater than 5 million ^{87}Rb atoms and a cloud temperature near 200 μK. The six laser cooling and repump beams are produced solely by the PIC and retroreflector mirrors, eliminating the need for bulk optics for beam collimation, splitting, and shaping. In the future, the retroreflectors can be replaced with smaller diameter optics mounted in a compact assembly closer to the glass cell or with a planar meta-surface retroreflector[59]. The power balance between the PIC beams does not noticeably drift during the operation and using a polarization-maintaining packaged fiber can reduce polarization-related

power drift. For precise and active beam power balancing, thermal tuner Si₃N₄ phase shifters[60] or ultra-low-power stress-optic piezo tuners[51] can be utilized. The single connectorized fiber input into the PIC makes this system amenable to combining multiple laser sources for beam delivery and can scale to more sophisticated applications that require several beams for trapping, repumping, probing, and narrow-line cooling[6] such as in state-of-the-art Sr neutral atom clocks[7]. Reducing the loss from the input fiber to the PIC-delivered beams is an important next step to reduce requirements for the source laser power. The PIC losses can be lowered by optimizing the performance of the individual components including the input fiber-to-waveguide taper, three-way splitter, slab mode expander, and shallow-etch grating. We estimate that with the results reported in literature[61] and with recent PIC test structures in our fabrication facility, we can reduce the total beam delivery loss to below 8 dB (see Supplemental Information Note 4). This level of performance eliminates the need for expensive optical amplifiers, allowing for total cooling beam intensity delivered to the atoms to reach the I_{sat} for ^{87}Rb for an input fiber-coupled power of 2 mW which can be produced directly with a commercial single-frequency diode laser.

The PICMOT system has a modular and robust design that can be used for a variety of cold atom experiments. For example, the large beam intersection height allows for the PIC to be held *ex vacuo* enabling using this beam delivery approach with different vacuum cells and eliminating breaking of vacuum to swap the PIC. Due to the large silicon nitride transparency window of 405 nm – 2350 nm[49], the PIC can be readily adapted for other visible wavelengths by changing the waveguide width in the lithography mask opening the potential for cooling of other atomic species and transitions such as cesium and strontium atoms[6]. Prior work has demonstrated grating emitters with a 90 degree angle from the PIC surface[46] and our grating design can be modified to vertically probe the trapped atom cloud for spectroscopy, atom interferometry, or an optical atomic clock. Generating multiple free-space beams from a single PIC provides an inherent stability of the optical paths which has been demonstrated to improve vibration tolerance in trapped-ion quantum computing[47]. These advantages can be beneficial in compact cold atom interferometer sensors such as for field-deployed gravity mapping measurements[19]. The PIC could deliver both the MOT and Raman probe beams and the uniform Raman beam spatial profile can improve the resulting interferometer sensitivity[62].

Compact, microfabricated 3D-MOTs are constrained by the scaling of the trapping beam overlap volume. The peak number of trapped atoms for different beam overlap volumes scales as $N \propto V^2$ for a pyramid MOT[38] and $N \propto V^{1.2}$ for a GMOT[34]. Ultimately, with uncorrelated particles the sensitivity of any cold atom experiment, such as atom interferometry, is limited by the quantum projection noise[29]. With a typical requirement of over 1 million atoms (corresponding to a phase resolution of a milliradian), the comparable GMOT configuration scaling implies that a minimum overlap volume of 45 mm³ is necessary[30]. In our PIC-based 3D-MOT the estimated beam overlap volume is 17.3 mm³. This is 9 times smaller than the volume used for an equivalent atom number GMOT which requires an input free-space beam of diameter 20 mm[20,34] (see Supplementary Figure 6). Our simulations show that for our existing slab expander, we can achieve output beam widths over 6 mm, which we estimate can achieve traps of over 10^7 atoms. A comparison of different integrated MOT beam delivery platforms and their performance is shown in Table 1. For techniques that achieve practical atom numbers of over 1 million, a constraint on the size of the cold atom package is the distance required for the beam expansion optics between the optical fiber input and the trap center. For example, GMOT demonstrations have used an input free-space beam with ~20 mm diameter beam that can be achieved with a commercial fiber collimator and bulk-

optic beam expander, taking up a length of over 10 cm. Similarly, while a meta-surface beam expander can be connected above a PIC, the propagation distance of 15 cm[36] to achieve the large beam size similarly limits package volume.

Future versions of the PICMOT system can introduce higher levels of system integration, reduced optical losses, and compact magnetic field generation[37]. Because the PIC fabrication process uses photolithography masks which can be flexibly configured, the chip component layout can be modified to include free space beam emitters of varying dimensions and beam emission angles. By extending the grating emitter design to two dimensions one can achieve control of the output beam polarization to eliminate quaterwaveplates[63]. Thermal or stress-optic tuners and phase can be incorporated to control beam parameters to maximize MOT atom numbers which can be compatible with on-line multi-parameter optimization algorithms[64]. The CMOS foundry compatible fabrication process also lends itself to hybrid integration of beam delivery with on-chip laser and detector technology[41]. Further integration with narrow linewidth lasers[50,53,65] can enable compact MOTs in which all the laser delivery, interrogation and probing is combined into a PIC. An example integrated atomic-photonic system for cold atoms is shown in Figure 4. The laser sources, reference cavities for laser stabilization[53,66,67], modulators[51], and free-space beam outputs can be co-located on a single PIC. Lasers used for MOT cooling, repumping, and probing can be stabilized and controlled, forming PIC-based "beam-lines" associated with each wavelength tailored to different frequency stability and control requirements. For example, by combining on-chip modulation and filtering[48], the probe beam can be shuttered to miniaturize the MOT cloud temperature measurement which is a common cold atom sensor readout step. This higher level of integration can facilitate the transition of atomic systems out of conventional laboratories to field-deployable systems as well as lower the cost of cold atom experiments.

Table 1. Summary of integrated beam delivery methods for 3D MOT cold atom systems.

Beam delivery method	Beam properties	Trapping beam overlap volume	Beam delivery distance[1]	Atom number
Conventional MOT with 6 free-space beams[30]	Collimated Gaussian beams, diameters ~30mm	~10^4 mm^3	N/A	~10^8
Diffraction grating MOT[34]	Input FS beam 20 mm diameter	10^3 mm^3	16 cm	6×10^7
Pyramid[38]	Input beam 4.2 mm diameter	10 mm^3	3 cm	10^4
PIC emitter, MS, GMOT[36]	Diverging beam after MS. Diameter 20 mm, flat-top	340 mm^3	15 cm	3×10^6
Large-area beams produced by SiN PIC (this work)	**2.5 x 3.5 mm^2, uniform intensity**	**17 mm^3**	**4 cm**	**5×10^6**

[1]Approximate distance for beam expansion and routing between a single fiber-coupled input and the trap center.

REFERENCES

1. Ashkin, A. & Gordon, J. P. Cooling and trapping of atoms by resonance radiation pressure. *Opt. Lett.* **4**, 161–163 (1979).

2. Chu, S., Hollberg, L., Bjorkholm, J. E., Cable, A. & Ashkin, A. Three-dimensional viscous confinement and cooling of atoms by resonance radiation pressure. *Phys. Rev. Lett.* **55**, 48–51 (1985).

3. Cohen-Tannoudji, C. N. Nobel Lecture: Manipulating atoms with photons. *Rev. Mod. Phys.* **70**, 707–719 (1998).

4. Adams, C. S. & Riis, E. Laser cooling and trapping of neutral atoms. *Prog. Quantum Electron.* **21**, 1–79 (1997).

5. Nicholson, T. L. *et al.* Systematic evaluation of an atomic clock at $2 \times 10{-}18$ total uncertainty. *Nat. Commun.* **6**, 6896 (2015).

6. Ludlow, A. D., Boyd, M. M., Ye, J., Peik, E. & Schmidt, P. O. Optical atomic clocks. *Rev. Mod. Phys.* **87**, 637–701 (2015).

7. Bloom, B. J. *et al.* An optical lattice clock with accuracy and stability at the $10{-}18$ level. *Nature* **506**, 71–75 (2014).

8. Lodewyck, J., Westergaard, P. G. & Lemonde, P. Nondestructive measurement of the transition probability in a Sr optical lattice clock. *Phys. Rev. A* **79**, 061401 (2009).

9. Lett, P. D., Julienne, P. S. & Phillips, W. D. Photoassociative Spectroscopy of Laser-Cooled Atoms. *Annu. Rev. Phys. Chem.* **46**, 423–452 (1995).

10.   Li, W., Mourachko, I., Noel, M. W. & Gallagher, T. F. Millimeter-wave spectroscopy of cold Rb Rydberg atoms in a magneto-optical trap: Quantum defects of the ns, np, and nd series. *Phys. Rev. A* **67**, 052502 (2003).

11.   Chin, C., Vuletić, V., Kerman, A. J. & Chu, S. High Resolution Feshbach Spectroscopy of Cesium. *Phys. Rev. Lett.* **85**, 2717–2720 (2000).

12.   Corbett, J. C. *et al.* Spanner: Google's Globally Distributed Database. *ACM Trans. Comput. Syst.* **31**, 8:1-8:22 (2013).

13.   Bloch, I. Quantum coherence and entanglement with ultracold atoms in optical lattices. *Nature* **453**, 1016–1022 (2008).

14.   Ladd, T. D. *et al.* Quantum computers. *Nature* **464**, 45–53 (2010).

15.   Jaksch, D. & Zoller, P. The cold atom Hubbard toolbox. *Ann. Phys.* **315**, 52–79 (2005).

16.   Saffman, M. Quantum computing with atomic qubits and Rydberg interactions: progress and challenges. *J. Phys. B At. Mol. Opt. Phys.* **49**, 202001 (2016).

17.   Bao, X.-H. *et al.* Efficient and long-lived quantum memory with cold atoms inside a ring cavity. *Nat. Phys.* **8**, 517–521 (2012).

18.   Bongs, K. *et al.* Taking atom interferometric quantum sensors from the laboratory to real-world applications. *Nat. Rev. Phys.* **1**, 731–739 (2019).

19.   Stray, B. *et al.* Quantum sensing for gravity cartography. *Nature* **602**, 590–594 (2022).

20.   Lee, J. *et al.* A compact cold-atom interferometer with a high data-rate grating magneto-optical trap and a photonic-integrated-circuit-compatible laser system. *Nat. Commun.* **13**, 5131 (2022).

21.   Kitching, J. Chip-scale atomic devices. *Appl. Phys. Rev.* **5**, 031302 (2018).

22.   Liu, L. *et al.* In-orbit operation of an atomic clock based on laser-cooled 87Rb atoms. *Nat. Commun.* **9**, 2760 (2018).

23.   Metcalf, H. J. & van der Straten, P. Laser Cooling and Trapping of Neutral Atoms. in *The Optics Encyclopedia* (John Wiley & Sons, Ltd, 2007). doi:10.1002/9783527600441.oe005.

24.   Phillips, W. D. Nobel Lecture: Laser cooling and trapping of neutral atoms. *Rev. Mod. Phys.* **70**, 721–741 (1998).

25.   Raab, E. L., Prentiss, M., Cable, A., Chu, S. & Pritchard, D. E. Trapping of Neutral Sodium Atoms with Radiation Pressure. *Phys. Rev. Lett.* **59**, 2631–2634 (1987).

26.   Chu, S. Nobel Lecture: The manipulation of neutral particles. *Rev. Mod. Phys.* **70**, 685–706 (1998).

27.   Steane, A. M., Chowdhury, M. & Foot, C. J. Radiation force in the magneto-optical trap. *J. Opt. Soc. Am. B* **9**, 2142 (1992).

28.   Gibble, K. E., Kasapi, S. & Chu, S. Improved magneto-optic trapping in a vapor cell. *Opt. Lett.* **17**, 526–528 (1992).

29.   Hoth, G. W., Donley, E. A. & Kitching, J. Atom number in magneto-optic traps with millimeter scale laser beams. *Opt. Lett.* **38**, 661 (2013).

30.   Rushton, J. A., Aldous, M. & Himsworth, M. D. Contributed Review: The feasibility of a fully miniaturized magneto-optical trap for portable ultracold quantum technology. *Rev. Sci. Instrum.* **85**, 121501 (2014).

31.   Lee, K. I., Kim, J. A., Noh, H. R. & Jhe, W. Single-beam atom trap in a pyramidal and conical hollow mirror. *Opt. Lett.* **21**, 1177–1179 (1996).

32.   Kohel, J. M. *et al.* Generation of an intense cold-atom beam from a pyramidal magneto-optical trap: experiment and simulation. *JOSA B* **20**, 1161–1168 (2003).

33.   Vangeleyn, M., Griffin, P. F., Riis, E. & Arnold, A. S. Laser cooling with a single laser beam and a planar diffractor. *Opt. Lett.* **35**, 3453–3455 (2010).

34.   Nshii, C. C. *et al.* A surface-patterned chip as a strong source of ultracold atoms for quantum technologies. *Nat. Nanotechnol.* **8**, 321–324 (2013).

35.   McGilligan, J. P. *et al.* Grating chips for quantum technologies. *Sci. Rep.* **7**, 384 (2017).

36.   McGehee, W. R. *et al.* Magneto-optical trapping using planar optics. *New J. Phys.* **23**, 013021 (2021).

37.   Chen, L. *et al.* Planar-Integrated Magneto-Optical Trap. *Phys. Rev. Appl.* **17**, 034031 (2022).

38.   Pollock, S., Cotter, J. P., Laliotis, A., Ramirez-Martinez, F. & Hinds, E. A. Characteristics of integrated magneto-optical traps for atom chips. *New J. Phys.* **13**, 043029 (2011).

39.   Zhu, L. *et al.* A dielectric metasurface optical chip for the generation of cold atoms. *Sci. Adv.* **6**, eabb6667 (2020).

40.   Blumenthal, D. J., Heideman, R., Geuzebroek, D., Leinse, A. & Roeloffzen, C. Silicon Nitride in Silicon Photonics. *Proc. IEEE* **106**, 2209–2231 (2018).

41.   Blumenthal, D. J., Heideman, R., Geuzebroek, D., Leinse, A. & Roeloffzen, C. Silicon Nitride in Silicon Photonics. *Proc. IEEE* **106**, 2209–2231 (2018).

42.   Newman, Z. L. *et al.* Architecture for the photonic integration of an optical atomic clock. *Optica* **6**, 680–685 (2019).

43.   Chauhan, N. *et al.* Ultra-low loss visible light waveguides for integrated atomic, molecular, and quantum photonics. *Opt. Express* **30**, 6960–6969 (2022).

44.   Kim, S. *et al.* Photonic waveguide to free-space Gaussian beam extreme mode converter. *Light Sci. Appl.* **7**, 72 (2018).

45.   Chauhan, N. *et al.* Photonic Integrated Si3N4 Ultra-Large-Area Grating Waveguide MOT Interface for 3D Atomic Clock Laser Cooling. in STu4O.3 (Optical Society of America, 2019). doi:10.1364/CLEO_SI.2019.STu4O.3.

46.   Hummon, M. T. *et al.* Photonic chip for laser stabilization to an atomic vapor with 10^-11 instability. *Optica* **5**, 443–449 (2018).

47.   Niffenegger, R. J. *et al.* Integrated multi-wavelength control of an ion qubit. *Nature* **586**, 538–542 (2020).

48.   Huffman, T. A. *et al.* Integrated Resonators in an Ultralow Loss Si3N4/SiO2 Platform for Multifunction Applications. *IEEE J. Sel. Top. Quantum Electron.* **24**, 1–9 (2018).

49.   Blumenthal, D. J. Photonic integration for UV to IR applications. *APL Photonics* **5**, 020903 (2020).

50.   Gundavarapu, S. *et al.* Sub-hertz fundamental linewidth photonic integrated Brillouin laser. *Nat. Photonics* **13**, 60–67 (2019).

51.   Wang, J., Liu, K., Harrington, M. W., Rudy, R. Q. & Blumenthal, D. J. Silicon nitride stress-optic microresonator modulator for optical control applications. *Opt. Express* **30**, 31816–31827 (2022).

52.   Fan, Y. *et al.* Hybrid integrated InP-Si_3N_4 diode laser with a 40-Hz intrinsic linewidth. *Opt. Express* **28**, 21713–21728 (2020).

53.   Liu, K. *et al.* 36 Hz integral linewidth laser based on a photonic integrated 4.0 m coil resonator. *Optica* **9**, 770–775 (2022).

54.   Chiow, S. & Yu, N. Compact atom interferometer using single laser. *Appl. Phys. B* **124**, 96 (2018).

55.   Lett, P. D. *et al.* Observation of Atoms Laser Cooled below the Doppler Limit. *Phys. Rev. Lett.* **61**, 169–172 (1988).

56.   Ketterle, W., Durfee, D. S. & Stamper-Kurn, D. M. Making, probing and understanding Bose-Einstein condensates. in *Bose-Einstein Condensation in Atomic Gases* 67–176 (IOS Press, 1999).

57.   Russell, L., Kumar, R., Tiwari, V. B. & Nic Chormaic, S. Measurements on release–recapture of cold 85Rb atoms using an optical nanofibre in a magneto-optical trap. *Opt. Commun.* **309**, 313–317 (2013).

58.   Steck, Daniel A. Rubidium 87 D Line Data. (2021).

59.   Arbabi, A., Arbabi, E., Horie, Y., Kamali, S. M. & Faraon, A. Planar metasurface retroreflector. *Nat. Photonics* **11**, 415–420 (2017).

60. Dong, M. *et al.* High-speed programmable photonic circuits in a cryogenically compatible, visible–near-infrared 200 mm CMOS architecture. *Nat. Photonics* **16**, 59–65 (2022).

61. Puckett, M. W. & Krueger, N. A. Broadband, ultrahigh efficiency fiber-to-chip coupling via multilayer nanophotonics. *Appl. Opt.* **60**, 4340 (2021).

62. Mielec, N. *et al.* Atom interferometry with top-hat laser beams. *Appl. Phys. Lett.* **113**, 161108 (2018).

63. Spektor, G. *et al.* Universal visible emitters in nanoscale integrated photonics. Preprint at http://arxiv.org/abs/2206.11966 (2022).

64. Tranter, A. D. *et al.* Multiparameter optimisation of a magneto-optical trap using deep learning. *Nat. Commun.* **9**, 4360 (2018).

65. Chauhan, N. *et al.* Visible light photonic integrated Brillouin laser. *Nat. Commun.* **12**, 4685 (2021).

66. Lee, H. *et al.* Spiral resonators for on-chip laser frequency stabilization. *Nat. Commun.* **4**, 2468 (2013).

67. Liu, K. *et al.* Photonic circuits for laser stabilization with integrated ultra-high Q and Brillouin laser resonators. *APL Photonics* **7**, 096104 (2022).

68. Bose, D., Wang, J. & Blumenthal, D. J. 250C Process for < 2dB/m Ultra-Low Loss Silicon Nitride Integrated Photonic Waveguides. 2 (2022).

DISCLAIMER

The authors declare no competing financial interest.

CONTRIBUTIONS

A.I., N. C., and D. J. B. prepared the manuscript. N. C. and D. J. B. contributed to the laser cooling PIC designs and N.C. simulated the photonic structures. D. B. performed the laser cooling PIC fabrication and J.W. diced the chips. A.I. and N.C. performed the PIC beam profile measurements and built the laser stabilization system. A.I. performed the PICMOT assembly, cooling demonstration, and the MOT characterization. A.I. analyzed data to extract the MOT atom number and temperature. D. J. B and P. D. K. supervised and led the scientific collaboration.

DATA AVAILABILITY

The data that support the plots within this paper and other finding of this study are available from the corresponding author on reasonable request.

ACKNOWLEDGEMENTS

METHODS

PIC design and modeling. The 780 nm single mode waveguide design is a 400 nm wide, 120 nm thick Si_3N_4 waveguide core with a 15 μm thick thermal oxide lower cladding layer and 3 um thick PECVD oxide upper cladding layer (see Supplementary Fig. 2 (a)). The 1 x 3 multi-mode-interference (MMI) device splits the guided 780 nm light into three single mode waveguides each coupled to a long 2D mode expander that increases the guided mode lateral dimension to 4 mm. Each 2D mode expander is terminated into an ultra-large area grating emitter of dimensions 4 mm x 5 mm to create the cooling beams. The 120 nm thick Si_3N_4 core slab design is chosen to match the single mode waveguide design, maintain low losses, and realize a compact mode expander. A side view diagram of the mode expander and grating emitter is shown in Supplementary Fig. 2 (b). The large beam size achieved is due to the large beam expansion in the x and y axes due to the design and performance of the slab expander and the grating emitter, respectively. The slab expander must be sufficiently wide such that the optical mode does not interact with the slab sidewalls and long enough to expand the mode to reach the target beam width. The large size of

this photonic structure is made possible by the low optical losses in our SiN platform and this design can be scaled to larger beam expansion. The grating is etched into the Si_3N_4 slab waveguide core, where the 10 nm partial etch depth was designed to provide the 54.7° diffraction angle and high power in the desired diffraction order. The combination of the shallow, controllable grating etch in the relatively thick 120 nm core enables a large beam size in the other axis. The chirped apodized grating is designed with a lens-like phase curvature profile to produce uniform beam intensity[45]. The grating coupling strength is lowest at the grating input and progressively increases as the light propagates in the grating region. The grating period and duty cycle are designed to range from 1.18 um to 1.08 um and 10% to 50% from front to end of the grating respectively. For more information about the design choices see Supplementary Information Note 3.

Fabrication process. The fabrication process (Supplementary Fig. 1) is CMOS foundry compatible[41] and starts with a 1 mm thick 100 mm (4-inch) diameter silicon wafer with 15 μm of thermal oxide. The waveguide core layer is made by depositing 120 nm of Si_3N_4 using Inductively Coupled Plasma-Plasma Enhanced Chemical Vapour Deposition (ICP-PECVD) at UCSB. The waveguide layer is first patterned using a standard 248 nm deep ultraviolet (DUV) stepper. The silicon nitride is then etched with an Inductively Coupled Plasma-Reactive Ion Etcher (ICP-RIE) using an optimized $CHF_3/CF_4/O_2$ etch chemistry developed at UCSB[45,68]. The wafer is then thoroughly cleaned and the process is repeated for the grating layer using a lower RF power during the ICP-RIE etch. The target etch depth for these gratings is 10 nm. After a final clean, ICP-PECVD is used to deposit 3 μm of SiO_2 upper cladding. The wafer is diced to access facets for fiber edge-coupling.

MOT demonstration. The beam delivery PIC is bonded to an aluminum plate and fiber packaged. Conventional zero-order quartz quarter waveplates are placed in a plastic holder layer directly above the PIC and rotated to achieve the required handedness and ellipticity of polarization. The PIC setup is mounted on a multi-axis stage and aligned with respect to a pair of anti-Helmholtz coils. A commercially available vacuum vapour cell containing a rubidium dispenser (the ColdQuanta™ rubidium miniMOT) is brought into the setup and mounted directly above the PIC. Two separate lasers were used for the cooling demonstration. The cooling laser is a Distributed Bragg Reflector (DBR) 780 nm laser (from Photodigm™) and the repump is derived from frequency-doubling a 1560 nm external cavity diode laser. The cooling laser is locked to the ^{87}Rb $5S_{1/2}, F = 2 \rightarrow F' = (1,3)$ cross-over transition and an acousto-optical frequency shifter (AOFS) is used to shift the cooling beam to a red detuning of 10-20 MHz relative to the $F = 2 \rightarrow F' = 3$ hyperfine transition (see Supplementary Fig. 3). Both beams are combined with a fiber-based coupler and amplified using a booster optical amplifier (BOA, Thorlabs BOA785S) for PIC input powers up to 80 mW. The BOA is used for MOT operation during the TOF measurements because of its ability to shutter the optical output with a switch-off time of less than 5 μs. For atom number and loading rate measurements, a fiber-coupled tapered amplifier providing an output power of up to 150 mW (Newport™) is used and the fluorescence of the MOT cloud is focused onto a photodetector. The MOT temperature is measured with absorption imaging by using a separate free-space probe beam that near-resonant with the $F = 2 \rightarrow F' = 3$ generated using another AOFS. During the TOF expansion and imaging, the PICMOT magnetic field and the cooling and repumping light is turned off. There were no additional cooling stages in this MOT demonstration.
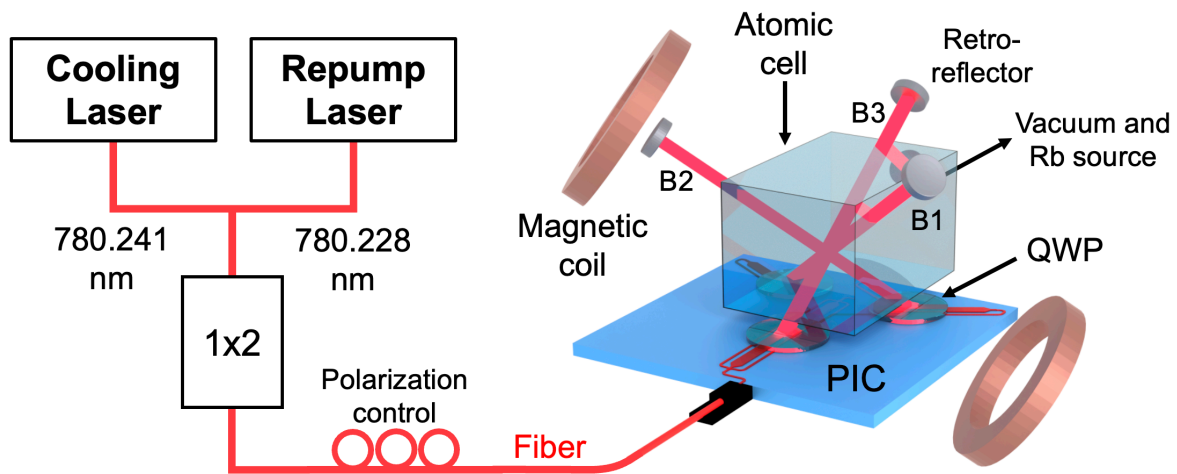
Fig. 1. PICMOT system. Laser cooling beam delivery PIC installed in the 3D MOT setup. The cooling and repump lasers are combined in a fiber coupler and connected to the PIC fiber input. The polarization is adjusted with a polarization controller. The quarter waveplate (QWP) holder layer is placed on the PIC and the stray-light filtering layer (not shown) is above the QWP holder. The PIC is placed under the glass cell containing the rubidium atoms and the magnetic field coils are aligned along beam B2 (the other beams are labeled B1 and B3). Retro-reflector mirror mounts are mounted above and used to overlap the counter-propagating beams.
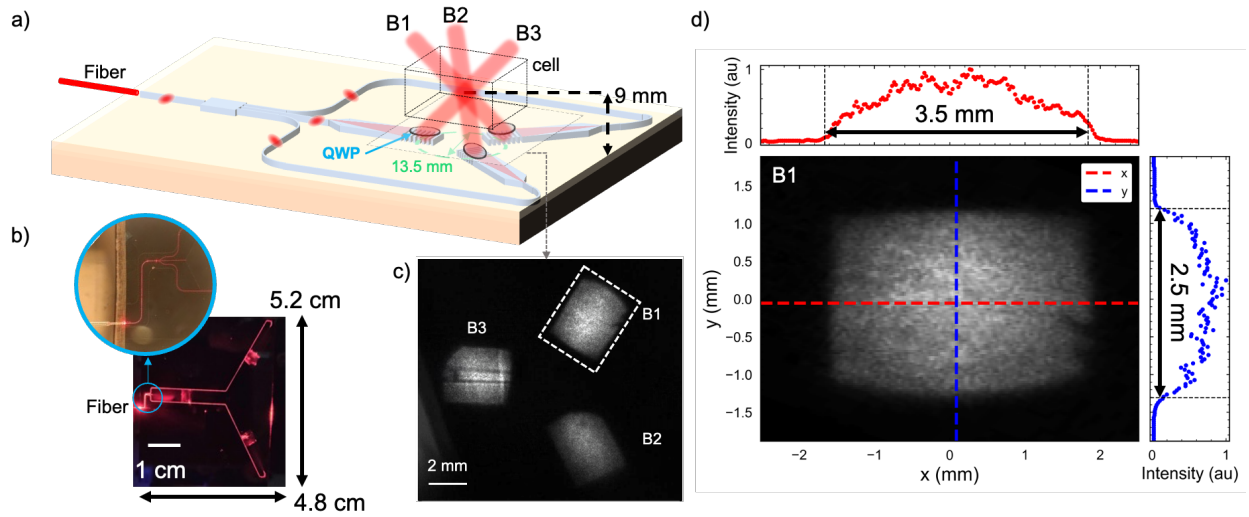
Fig. 2. Laser cooling beam delivery PIC. a) Layout of the laser cooling beam delivery PIC used to generate free-space beams for the 3D MOT. Fiber-coupled light is guided to a splitter and directed to the mode expanders and grating emitters. Bulk quarter waveplates are placed directly above each emitter. The dashed rectangle represents the height at which the beam profile is imaged. b) PIC illuminated with red laser light to demonstrate the light propagation. The inset shows the MMI splitter and fiber coupling. c) Image of the PIC beams incident on the paper sheet held parallel to the PIC surface at a height of 5 mm. The non-uniformity beam B3 is discussed in the Supplementary Information. d) Perpendicular cross-section image of beam B1 and the profiles of the beam intensity for two axes of the beam emitter and the corresponding $1/e^2$ beam widths.
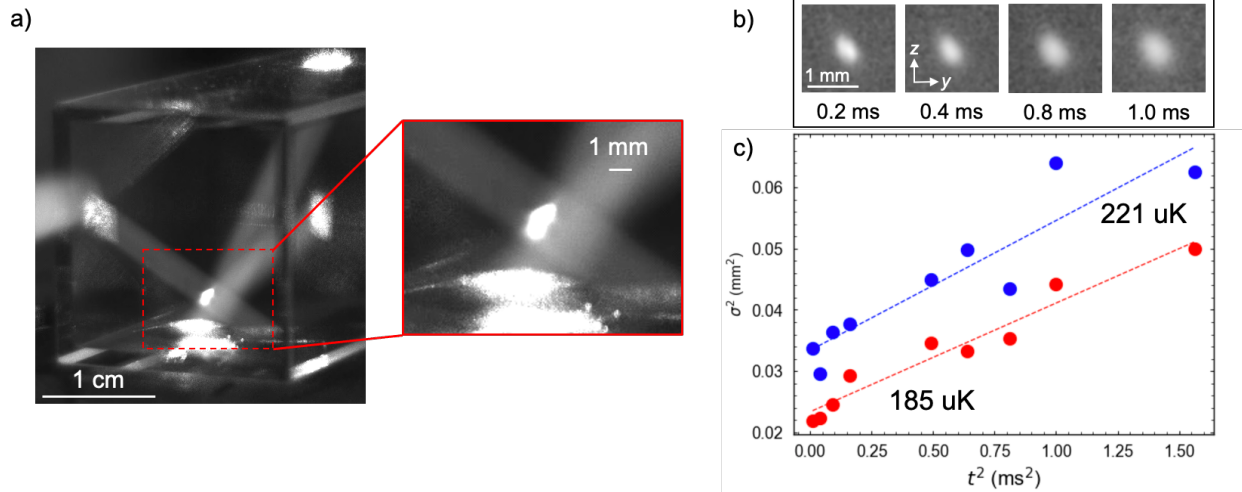
Fig. 3. Rubidium 3D MOT demonstration. a) View from a camera located on the side of the PICMOT setup. The side length of the glass cell is 20 mm. The trapping beams fluoresce as they propagate through the cell containing the atomic vapor. Inset: zoom-in of the MOT cloud (note some camera pixels are saturated). b) Averaged absorption images of the MOT cloud after free-expansion over several times. c) Squared cloud radius in the z (blue) and y (red) dimensions for squared TOF times t^2. The linear fits are for $\sigma^2 = \sigma_0^2 + \frac{k_B T}{m} t^2$, where σ is the Gaussian width (radius) of the cloud along an axis, k_B is the Boltzmann constant, m is the mass of a single ^{87}Rb atom, and T is the temperature.
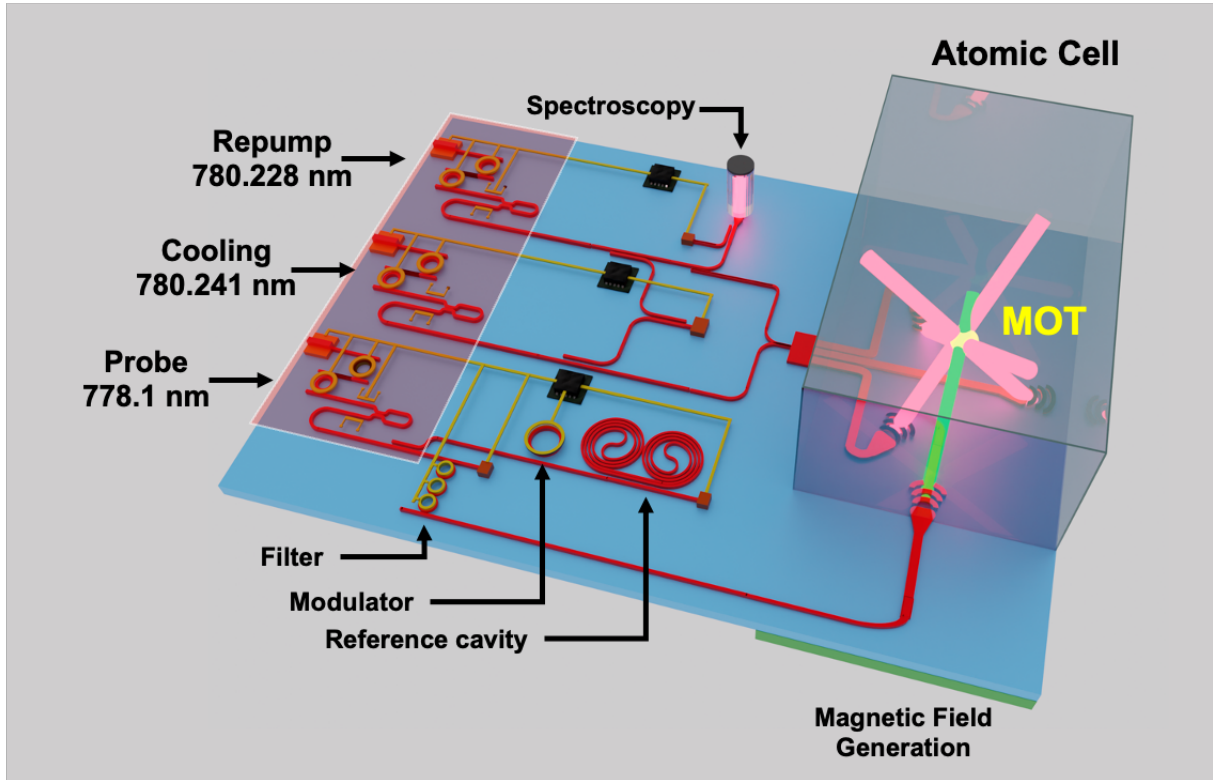
Fig. 4. Example integration application of PIC to free-space beam delivery. Illustrative example of how the large-area PIC beam emitters can be used in an integrated atomic-photonic system for cold atom trapping and probing. Heterogeneously integrated external cavity Si_3N_4 lasers[52] can be used to generate light for atom cooling, repumping, and probing. The lasers are each stabilized to a spectroscopy reference and a probe laser is locked to a reference cavity coil resonator for frequency noise reduction. PZT-actuated[51] modulators and shutters can be utilized for locking and probe light control. Each laser beam-line is delivered to the atomic species using the large-area photonic grating emitters of this work. The vacuum cell containing the atoms and the magnetic field generation layer can be planar integrated around the photonic chip.

Supplementary Information

Photonic integrated beam delivery in a rubidium 3D magneto-optical trap

Andrei Isichenko[1], Nitesh Chauhan[1], Debapam Bose[1], Jiawei Wang[1], Paul D. Kunz[2], and Daniel J. Blumenthal[1*]

[1] Department of Electrical and Computer Engineering, University of California Santa Barbara, Santa Barbara, CA 93106 USA

[2] U.S. Army Research Laboratory, Adelphi, MD 20783 USA

* Corresponding author (danb@ucsb.edu)

Supplementary Note 1: Introduction

In this Supplementary Information, we discuss further details with respect to the laser cooling beam delivery PIC device fabrication process, including the waveguide, slab expander, and grating emitter design. We also describe more about the PIC optical losses, strategies for loss reduction, beam profiles, and operation and characterization of the MOT.
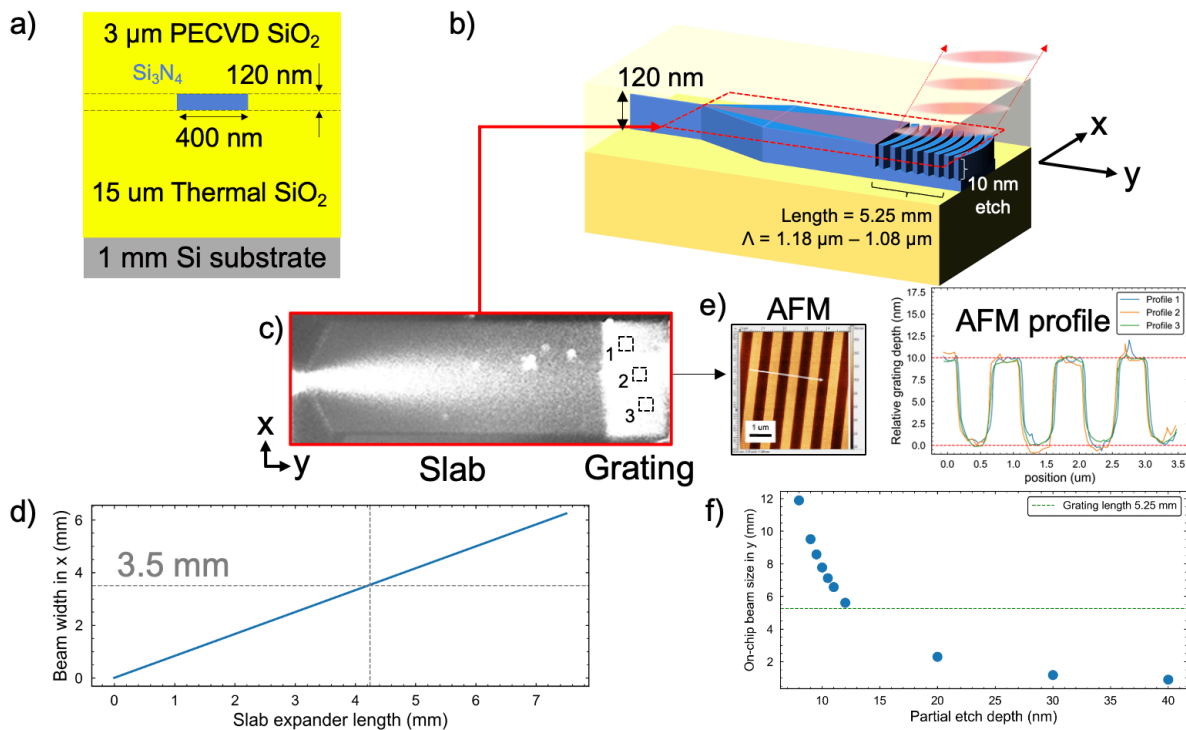
Supplementary Note 2: Beam delivery device fabrication
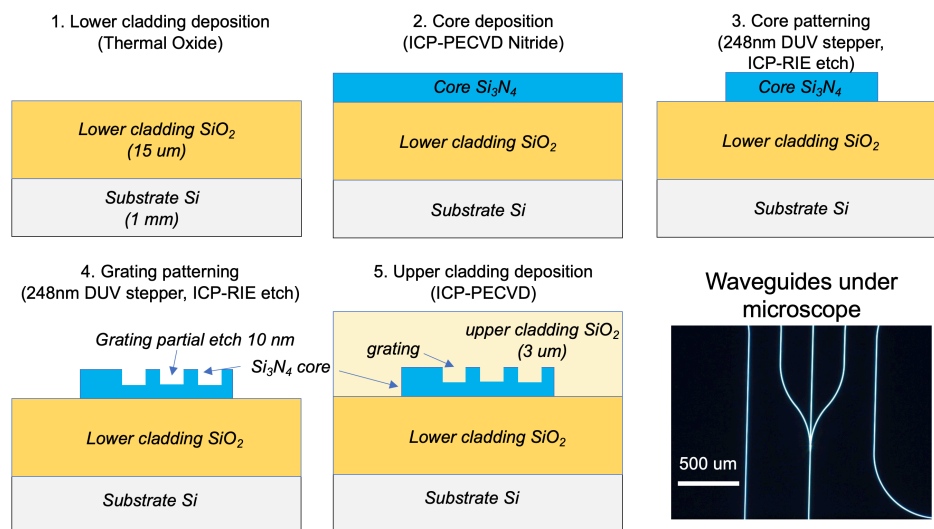
Supplementary Fig. 1. Beam delivery PIC fabrication process flow. Step 1: lower SiO_2 cladding deposition. Step 2: Silicon nitride core deposition. Step 3: Silicon nitride core etch. Step 4: grating layer partial etch. Step 5: Upper oxide cladding deposition. Image of the 1x3 splitter of the fabricated PIC.

Exposure calibration procedure. To calibrate the lithography steps for the waveguide and grating etches, two sets of focus exposure array jobs with the ASML PAS 5500 stepper tool were done using a wafer with silicon nitride on top of thermal oxide on a silicon substrate. The doses of the center elements were 16 mJ/cm² and 25 mJ/cm², respectively. The focus offset difference between the elements was 0.2 μm for both. An image quality control (IQC) procedure was run on the tool to ensure that the absolute focus exposure correction while running a job would be less than 20 nm. After development of the resist and etching of the antireflective coating layer, the nitride layer was etched with our standard recipes for the waveguide and grating etches[1,2], as shown in Supplementary Fig. 1. Subsequently, the wafer was cleaned and measurements of the waveguide and grating dimensions were taken with a SEM. The elements of the focus exposure array with the best quality were used to inform the conditions for the PIC devices of this work.

Supplementary Note 3: Beam delivery device design

Supplementary Fig. 2. Beam delivery device design. a) Waveguide dimension for single-mode operation at 780 nm. b) Slab expander and grating emitter. c) Image of the slab expander grating emitter illuminated with 780 nm light. d) Simulation of the slab expander rate of beam expansion. The expander enables reaching an on-chip beam width of 3.5 mm after 4.2 mm of expansion. e) AFM images at three profile locations shows that the grating emitter partial etch depth is relatively uniform across the emitter. f) Simulation of achievable on-chip beam size in the y dimension for different grating partial etch depths.

Waveguide and slab expander design. The waveguide is designed to support a single TE0 mode, have low loss, have bend radius <500um and provide a short slab expander length while maintaining low losses. The waveguide cross section is shown in Supplementary Fig. 2(a). To achieve the required beam sizes for the MOT, we introduce a waveguide-to-slab mode transition within our chip. The slab expander is a wide slab of Si₃N₄ which allows the mode to expand freely inside it. Different waveguide core thicknesses result in different length of beam expander due to

2

different effective refractive index of mode. For lower losses a thinner core is preferred[3] but that results in larger bend radii and longer slab expander. A thinner core results in very long tapers which are impractical, whereas a thicker core helps in making the beam expander more compact due to higher index contrast. In addition, the bend radius is also considered as thinner cores have larger minimum bend radii resulting in larger devices. For our devices, we define minimum bend radius as the radius below which the loss contribution from the bend exceeds 0.01dB/m and we ensure to keep our bend radii larger than the minimum bend radius for a core geometry. Commercially available simulation software was used to model the expansion of beam inside the taper for different core thicknesses. The simulation was performed for core thicknesses 40 nm and 120 nm with waveguides designed for each core thickness entering a taper of identical length and width. The waveguides for the 40 nm and 120 nm core width were selected to support single TE mode. The mode was propagated using beam propagation method (BPM) to observe the mode diameter expansion in the slab. From simulation, the length of the slab required for a 4 mm beam width is extremely long (>20 mm) for a 40 nm core. The corresponding minimum length of slab required for 120 nm core is 4.2 mm (see Supplementary Fig. 2 (e)). A 120 nm core is chosen as it provides a compact slab expander and a bend (critical bend radius <500 um) that makes it possible to fit a single grating in one reticle while also having low 0.3 dB/cm loss. Based on results from a previous fabrication run we re-used a photolithography mask where the slab expander length was 11.43 mm. This length fits easily in a 21 mm x 25 mm reticle for our current mask without requiring stitching at the slab or grating section.

Grating design and modeling. The laser cooling beams are formed using three large-area, chip-to-free-space grating couplers. These couplers are formed in a material system composed of a silicon nitride device layer and two silicon dioxide cladding layers. Historically, grating couplers have been used in integrated photonics for a relatively small subset of tasks, the most well-known of which is likely the coupling of light between chip-scale waveguides and optic fibers[4]. Grating couplers are ideal for interfacing between planar devices and their surrounding environment. Due to the careful control over the grating's k-vector, the angle at which light is either emitted or transmitted can be targeted with a high degree of precision. When light propagating within a chip diffracts from a grating written into its path, the angle at which the light diffracts relative to the chip's surface normal may be calculated analytically. If we assume that the light is initially propagating within the x-y plane, and that the z-axis represents the direction normal to the chip's surface, then the diffraction angle is given as:

$$\theta = \tan^{-1}\left(\frac{\sqrt{k_{xo}^2 + k_{yo}^2}}{k_{zo}}\right) \, ,$$

where

$$k_{xo} = k_x - K_x$$
$$k_{yo} = k_y - K_y$$
$$k_{zo} = k_z - K_z$$

and $k_{zo} = \sqrt{(2\pi/\lambda)^2 - k_{xo}^2 - k_{yo}^2}$. In these expressions, k_x and k_y are the x- and y-components of the initial k-vector of the light, and K_x and K_y are the x- and y-components of the grating's k-vector, respectively. Additionally, k_{xo}, k_{yo}, and k_{zo} represent the three components of the diffracted light's k-vector in free-space. For the MOT, the three beams diffracted from the chip are required to each be orthogonal to one another. This requires that for each grating the diffraction angle relative to the surface normal equals 54.7° and the slabs spaced 120° apart from each other. The center of each grating emitter is placed on 13.5 mm circle to ensure the 9.45 mm intersection spot which enables enough clearance for waveplates and cell wall.

At the interface between the waveguide, which provides two-dimensional confinement, and the slab expander, which only provides confinement along one axis, the optical wave begins to diverge along the direction which is both transverse to its propagation and parallel to the chip's surface normal. This divergence can be represented mathematically as a spatially dependent distribution of optical k-vectors, given as:

$$k_x(x, y) = k_o \cos(y/x)$$
$$k_y(x, y) = k_o \sin(y/x)$$

In this expression, x and y are the coordinates within the nitride slab relative to the point at which the waveguide-to-slab transition occurs. This means that because the light is required to be emitted in a specific direction regardless of position, the grating coupler's k-vector must vary spatially to compensate for the varying components of the optical k-vector. This requirement may be represented mathematically as:

$$K_y = k_y = k_o \sin(\tan^{-1}(y/x))$$
$$K_y = k_y - k_o \sin(y/x)$$
$$K_x = k_x - \frac{k_o \tan(54.7°)}{\sqrt{1 + \tan(54.7°)}}$$

After these local maps of grating period and direction have been calculated, the spatially variant grating may be generated numerically by beginning a single grating line at a chosen starting point and "walking forward", iteratively defining its movement and width. This process may be repeated for an arbitrary number of grating lines until the chosen grating area has been defined. We thus generate curved gratings which take slab mode and produce a flat intensity profile in free space. Based on results from a previous fabrication run we re-used a photolithography mask with a grating length of 5.25 mm (corresponding to a cross-sectional beam width of 2.5 mm). The grating etch depth required for an on-chip beam width of 5.25 mm was simulated to be 12 nm in a 120 nm core. A 10 nm grating etch depth was chosen considering a potential 20% etch depth variation. Subsequent measurements of AFM show that the etch depth variation is smaller than expected (Supplementary Fig. 2(d)). The grating coupling strength is lowest at the grating input and

progressively increases as the light propagates in the grating region. The grating period and duty cycle are designed to progress from 1.18 um – 1.08 um and 10% - 50% from front to end of the grating respectively (Supplementary Fig. 2(b)).

Supplementary Note 4: Beam delivery device characterization and future improvements

Optical losses in the beam delivery. We measured the optical losses at each major component on another beam delivery PIC device of the same fabrication run (see Supplementary Table 1). The individual losses of facet, MMI, slab expander and grating were extracted by iteratively measuring and dicing the device in a cutback method. First, the loss of full-size device was measured. Next, the grating was diced from slab and an integrating sphere was used to measure the slab output and extract the grating loss. Finally, waveguide output without the slab was measured to extract the facet coupling loss. The propagation loss was measured by subtracting the facet loss from a long loop around waveguide. For the single grating emitter measured, the total loss from the waveguide input to the grating output beam was 12.5 dB. The MMI splitter excess loss was inferred from the performance of one of the beams of the PIC device used in this work.

The rightmost column of Supplementary Table 1 estimates the achievable losses in future beam delivery PIC designs based on simulations, test structure measurements, and values from literature. The MMI splitter excess losses originate from fabrication imperfections due to the small dimensions of MMI which in the future we will address by replacing the MMI with an evanescent coupler which we have measured to have <0.3 dB loss. The fiber-to-chip coupling loss can be reduced by using tapered mode matchers, facet polishing, or other mode-matching structures[5]. Next, our waveguide is designed to support a TE mode with an estimated loss of ~0.3 dB/cm. By increasing the waveguide width we can operate in TM mode which has been shown to achieve a lower loss[6]. We estimate that with a loss of 0.15 dB/cm we can achieve a total propagation loss of 0.7 dB. Lastly, the grating emitter output power is distributed over different diffracted orders which affects the overall beam delivery efficiency (Supplementary Figure 3(b)). We define the power in the target diffracted order as P_0 and the power in the other diffracted order (near vertical) as P_{+1} and a ratio $R = P_{+1}/P_0$. From simulation we find that we can improve the diffraction efficiency into the 0 order and reduce R by adjusting the grating partial etch depth. We find that at an optimal etch depth we can reach $R = 0.5$ (supplementary Figure 3(c)). Assuming that the fraction of total optical power delivered by the emitter is unchanged, we estimate that we can reduce the grating output loss by 1.1 dB. This requires accurate control of the etch depth and with proper calibration a tolerance of <0.5 nm can be achieved. Furthermore, our simulation predicts that for a 10 nm etch depth and a 5.25 mm length grating section, 20% of the power is not diffracted and scatters. By extending the grating length to 7 mm we predict that we can increase the diffracted power and reduce the total grating output loss by 1.7 dB. We estimate a total achievable beam deliver loss (input fiber to all three beams) of 7.2 dB. Further improvements may be possible by using a bottom reflector below the grating[7] and using grating inverse design[8].

Supplementary Table 1. Beam delivery loss budget.

Supplementary Information for Photonic integrated beam delivery in a rubidium 3D magneto-optical trap

Location on PIC	Measured Loss	Estimated Achievable Loss
Fiber to input waveguide	3.8 dB	0.3 dB[5]
1x3 splitter excess loss and waveguide propagation loss	3.3 dB	1.0 dB
Waveguide to slab expander	0.7 dB	0.7 dB
Slab to free-space grating output	8.0 dB	5.2 dB
Total beam delivery loss input fiber to all PIC beams	**15.8 dB**	**7.2 dB**
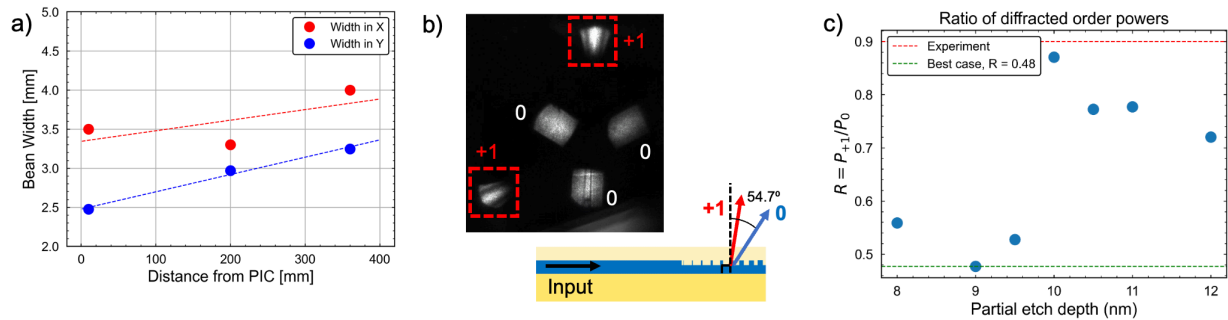
Supplementary Fig. 3. Grating emitter beam characterization. a) Measurements of the beam collimation for PIC beam 1 (B1). The beam has divergence angles of $0.16°$ and $0.35°$ in the x- and y-dimensions as defined in Figure 2(d) of the main text. The corresponding effective Rayleigh lengths are 125 and 113 cm in the x- and y- axes, respectively. b) Image of the higher-order mode for beams 2 and 3 (B2, B3) with imaging paper sheet above the beam intersection point. The +1 order for the third beam (not shown) has a similar profile. c) Simulation for ratio of power of diffracted orders for varying partial etch depths.

Beam collimation and intensity profile. The beams profile and angle of the intersecting beams was measured with a camera that imaged a translucent paper sheet held above the PIC surface at varying distances. The measured beam width (defined as the $1/e^2$ diameter) for beam B1 as a function of the distance from the emitter is shown in Supplementary Fig. 3 (a). We note that beam B3 has a non-uniformity in its intensity profile which we attribute to imperfect photolithography exposure which effectively reduced the width of the waveguide at the input to the slab expander. We attribute the fact that the MOT cloud is not centered inside the beam overlap volume to this beam non-uniformity.

Supplementary Note 5: MOT system and characterization
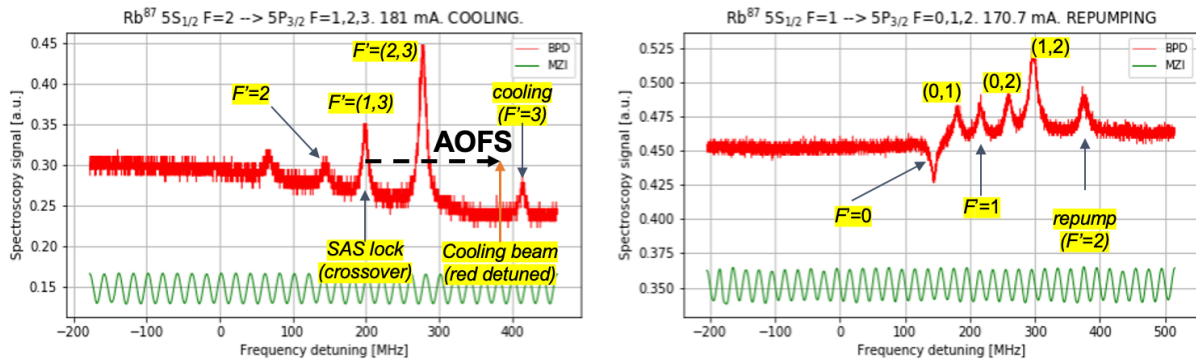
Supplementary Fig. 4. Laser stabilization for MOT demonstration. a) Frequency sweep of the cooling laser across the ^{87}Rb $5S_{1/2}$ $F = 2 \rightarrow 5P_{3/2}$ $F' = 1, 2, 3$ transitions. An acousto-optical frequency shifter (AOFS) is used to shift the laser locked to the $F' = (1,3)$ peak to achieve a red-detuning with respect to the $F' = 3$ cooling transition. An unbalanced Mach-Zehnder interferometer (MZI) with FSR 20 MHz is used to calibrate the laser frequency sweep while the saturation absorption spectroscopy signal is recorded on a balanced photodetector (BPD). b) Frequency sweep across the ^{87}Rb $5S_{1/2}$ $F = 1 \rightarrow 5P_{3/2}$ $F' = 0, 1, 2$ transitions. The repump laser is aligned to the $F' = 2$ cooling transition.

MOT laser system. A frequency sweep of the relevant ^{87}Rb *D2* line hyperfine transitions of the saturation absorption spectroscopy setup is shown in Supplementary Fig. 4. The cooling laser is frequency stabilized to a cross-over peak (left panel) and the acousto-optical frequency shifter (AOFS) is used to control the ~200 MHz shift for detuning adjustment. The repump laser is free-running and aligned with respect to the repump transition by maximizing the signal of the MOT fluorescence.

Characterization. We measure the MOT loading rate by capturing the fluorescence of the atoms onto a photodetector. The loading rate curve from which we extract the steady-state atom number and the loading time is shown in Supplementary Fig. 5.
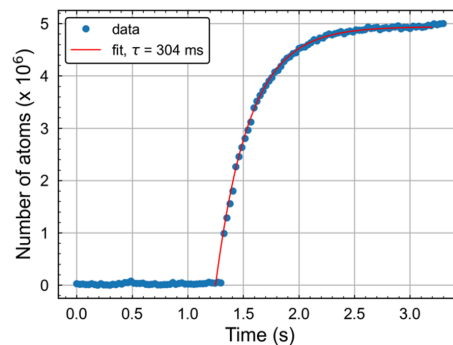
Supplementary Fig. 5. MOT loading rate measurement. MOT loading curve trace taken with a photodetector that captures the fluorescence of the MOT cloud. The magnetic field is turned on at $t = 1.25$ seconds. The data is fit to an exponential of the form $N(t) = N_{ss}(1 - \exp(-t/\tau))$ where N_{ss} is the steady-state atom number and τ is the loading time for the atoms in the trap. The loading rate is calculated at $\Gamma = 1/\tau = 3.33$ s^{-1}.

Supplementary Note 6: Comparison of integrated beam delivery methods for 3D MOT cold atom systems.

Atom number and trapping beam overlap volume. The number of atoms trapped in a MOT depends on the overlap volume of the cooling beams. This is because a larger beam volume in each dimension of the trap is related to the stopping distance available to cool the atoms and therefore the maximum speed of the atoms that can be part of the MOT. The beam overlap volume of our PIC-based beam delivery approach is 17.3 mm^3. This is 9 times smaller than the volume used for an equivalent atom number GMOT. Furthermore, these GMOTs utilize an input free-space beam of diameter 20 mm which requires beam expansion and collimation optics. Compared to microfabricated pyramid MOTs which have a comparable beam overlap volume of up to 20 mm^3, we achieve an atom number that is over 700 times higher.
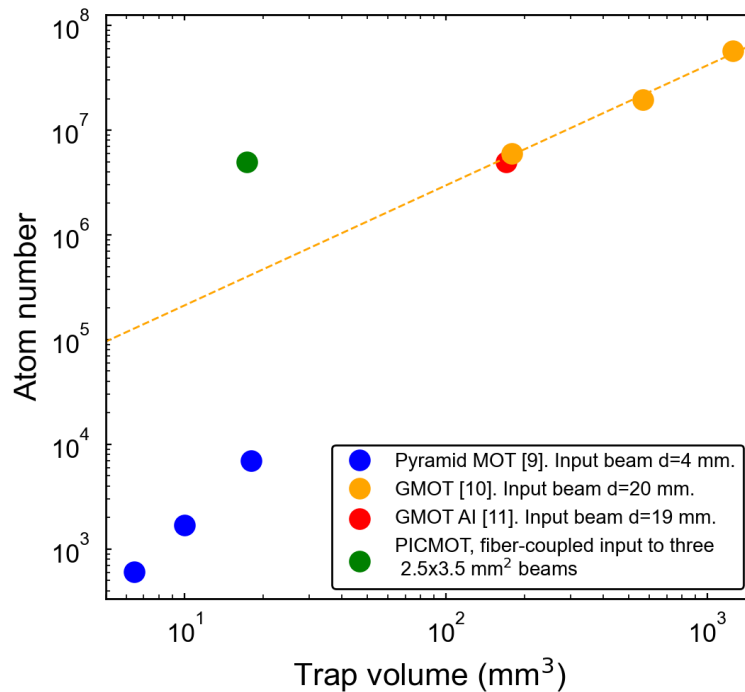
Supplementary Fig. 6. Atom numbers and cooling beam trapping volume for different integrated beam delivery methods. Blue: microfabricated pyramid chip MOTs (pyramid MOT)[9]. Orange: Diffraction grating MOT (GMOT) with an approximate scaling law[10]. Red: diffraction grating MOT used in a cold atom interferometer sensor[11]. Green: photonic-integrated-circuit MOT of this work.

References

1. Gundavarapu, S. *et al.* Sub-hertz fundamental linewidth photonic integrated Brillouin laser. *Nat. Photonics* **13**, 60–67 (2019).

2. Chauhan, N. *et al.* Photonic Integrated Si3N4 Ultra-Large-Area Grating Waveguide MOT Interface for 3D Atomic Clock Laser Cooling. in STu4O.3 (Optical Society of America, 2019). doi:10.1364/CLEO_SI.2019.STu4O.3.

3. Chauhan, N. *et al.* Ultra-low loss visible light waveguides for integrated atomic, molecular, and quantum photonics. *Opt. Express* **30**, 6960–6969 (2022).

4. Taillaert, D. *et al.* Grating Couplers for Coupling between Optical Fibers and Nanophotonic Waveguides. *Jpn. J. Appl. Phys.* **45**, 6071 (2006).

5. Puckett, M. W. & Krueger, N. A. Broadband, ultrahigh efficiency fiber-to-chip coupling via multilayer nanophotonics. *Appl. Opt.* **60**, 4340 (2021).

6. Liu, K. *et al.* Ultralow 0.034 dB/m loss wafer-scale integrated photonics realizing 720 million Q and 380 μW threshold Brillouin lasing. *Opt. Lett.* **47**, 1855–1858 (2022).

7. Zou, J. *et al.* Ultra efficient silicon nitride grating coupler with bottom grating reflector. *Opt. Express* **23**, 26305–26312 (2015).

8. Spektor, G. *et al.* Universal visible emitters in nanoscale integrated photonics. Preprint at http://arxiv.org/abs/2206.11966 (2022).

9. Pollock, S., Cotter, J. P., Laliotis, A., Ramirez-Martinez, F. & Hinds, E. A. Characteristics of integrated magneto-optical traps for atom chips. *New J. Phys.* **13**, 043029 (2011).

10. Nshii, C. C. *et al.* A surface-patterned chip as a strong source of ultracold atoms for quantum technologies. *Nat. Nanotechnol.* **8**, 321–324 (2013).

11.   Lee, J. *et al.* A compact cold-atom interferometer with a high data-rate grating magneto-optical trap and a photonic-integrated-circuit-compatible laser system. *Nat. Commun.* **13**, 5131 (2022).